Relation between convective thermal patterns and heat flux through an evaporating surface via 2D and 3D numerical simulations

Hatim Machrafi[1,a], Carlo S. Iorio[2,b], Pierre C. Dauby[1,c]

[1]University of Liège, Thermodynamics of Irreversible Phenomena, Allée du 6-Août, 17, 4000 Liège, Belgium

[2]Université Libre de Bruxelles, Microgravity Research Center, CP165/62, avenue F.D. Roosevelt, 50, 1050 Brussels, Belgium

[a]h.machrafi@ulg.ac.be, [b]ciorio@ulb.ac.be, [c]pc.dauby@ulg.ac.be

It is the purpose of this paper to investigate the temporal behavior of convection flow, pattern formation and heat flux through a liquid-gas interface for a pure liquid (HFE-7100) evaporating into a nitrogen gas flow. Two- and three-dimensional numerical fluid-dynamics simulations are performed using the software ComSol (finite elements method). This study is related to an experimental setup to be flown onboard the International Space Station (ESA "Evaporation Patterns" project). The two-dimensional results show that, due to the surface-tension variation with cooling, small rolls are formed near the liquid-gas interface, followed by the rolls growing into the bulk liquid, due to buoyancy. The three-dimensional results show that regular patterns are formed in the beginning accompanied by small fluctuations of the heat flux. Afterwards, these patterns transform into chaotic flow and the fluctuations of the heat flux attenuate. Nonetheless, the heat flux fluctuations deviate only slightly from the mean value.

Keywords: Thermal conduction, Thin liquid layers, Local thermodynamic equilibrium, Evaporation, Pattern formation, Heat flux.

Nomenclature

c_p	Heat capacity [J kg^{-1} K^{-1}]
D_g	Diffusion coefficient in the gas [m^2/s]
$\vec{g}$	Standard gravity constant [m/s^2]
h_{gas}	Liquid height [m]
h_{liq}	Gas height [m]
$\vec{J}$	Evaporation flux [kg m^{-2} s^{-1}]
L	Latent heat of evaporation [J/kg]
M	Molar mass [kg/mole]
n	Molar density [mole/m^3]
p	Pressure [Pa]
$\vec{q}$	Heat flux [W/m^2]
Q	Gas flow [m^3/s]
R	Universal gas constant [J mole^{-1} K^{-1}]
t	Time [s]
T	Temperature [K]
u	x-coordinate of the velocity field [m/s]
$\vec{v}$	Velocity field [m/s]
v	y-coordinate of the velocity field [m/s]
w	z-coordinate of the velocity field [m/s]
x	x-coordinate of the spatial system [m]
y	y-coordinate of the spatial system [m]
z	z-coordinate of the spatial system [m]

Greek letters

α	Thermal expansion coefficient [K^{-1}]
γ	Surface tension [N/m]
ε	Solutal expansion coefficient [-]

κ	Thermal diffusivity [m^2/s]
λ	Thermal conductivity [W m^{-1} K^{-1}]
μ	Dynamic viscosity [Pa s]
ρ	Density [kg/m^3]
χ	Molar fraction [-]
Subscripts	
0	Reference base state
amb	Ambient conditions
g	Gas phase
l	Liquid phase
sat	Saturation conditions
Σ	Liquid-gas interface

1. Introduction

Rayleigh-Bénard (RB) and Marangoni-Bénard (MB) convection of a fluid heated from below and/or cooled from above is a classical problem in fluid dynamics, e.g. "Pearson (1958)" and "Bénard (1901)". Its role has been important in the development of stability theory in hydrodynamics "Drazin and Reid (1981)" and has been quintessential in the study of patterns formation and spatial-temporal chaos "Bodenschatz et al. (2000)". RB and MB convection also play important roles in recent stability analyses where evaporation is the driving force "Machrafi et al. (2013a)" and "Bestehorn (2007)". From an applied viewpoint, thermally driven flows are of utmost importance. Examples are thermal convection in the atmosphere, in oceans, buildings, process technology, to mention a few. These thermal flows can give rise to certain self-sustained patterns that can be stationary or can change into other patterns or even to chaotic structures. We are here especially interested in evaporation-related thermal flows. These have already been studied theoretically, numerically and experimentally in several works "Bestehorn and Merkt (2006)", "Goncharova et al. (2013)", "Iorio et al. (2011)" and "Lyuling and Kabov (2014)". The present work falls into a general framework which consists of observing the behavior of patterns and structures that can be formed after instability onset in an evaporating liquid layer under a gas flow. In previous work, such a configuration has been studied with regard to theoretical instability thresholds "Machrafi et al. (2013b)". What is of interest here are two- and three-dimensional numerical simulations of the transient temperature and motion of a liquid evaporating into a horizontal nitrogen gas flow. The chosen liquid is HFE7100 (an electronics coolant liquid produced by 3M) and the gas is nitrogen. The numerical fluid dynamics simulations are performed using the software ComSol (finite elements method). The evaporation, taking place at the upper surface of the liquid layer results into the cooling of the liquid surface. This cooling induces temperature gradients in the liquid. These temperature gradients are in turn responsible for the development of a thermal boundary layer that develops from the liquid-gas interface into the bulk liquid. Since density and surface tension depend both on the temperature, the temperature gradients cause them to change. As a consequence, locally colder zones of fluid will have a higher density and surface tension than the neighboring fluid particles, which will cause the fluid to move. Surface-tension induced motion is referred to as Marangoni flow and buoyancy-driven flow as Rayleigh flow. When the thermal gradient exceeds a certain threshold, instability sets in and self-sustained regular convective patterns take place. As time proceeds, these patterns can become chaotic.

The numerical analysis in the present work is devoted to the evaporator part of the EVAPORATION PATTERNS (EP) (previously named CIMEX) experimental setup "Machrafi et al. (2013b)", developed by the European Space Agency (ESA) and to be flown in the International Space Station (ISS) shortly. Our work consists in a pre-flight analysis of the experiment, the goal of which is to quantify mass-transfer processes across interfaces, and to study their coupling with surface-tension driven (Marangoni) flows/convection and instabilities in a pure liquid and a mixture. In this work, we focus on fluid flow, pattern formation and heat flux. First, we will describe the system that the simulations will address. Then, we will consider the evolution of the fluid flow into the bulk liquid using 2D simulations, varying the liquid thickness. Finally, by means of 3D simulations, we will

investigate the time evolution of the relation between pattern formation and heat flux through the liquid-gas interface.

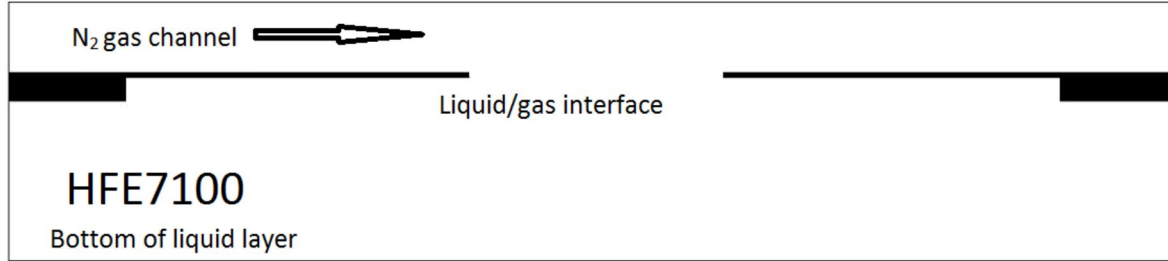## 2. Description of the system

2.1 Mathematical model

Fig. 1 Physical system.

Fig. 1 is a sketch of the physical system studied here. The system has a width and length 50 mm by 50 mm with a certain liquid height, h_{liq}, in this work variable from 2 mm to 8 mm. The evaporated liquid is constantly replenished from the bottom, so that the gas-liquid interface, present within an opening 10.6 mm by 10.6 mm, remains at the same level. Above it, there is a gas channel with a height, h_{gas}, of 3.0 mm and a width of 50 mm. In this channel, nitrogen flows with a rate, Q_{gas}, of 100 or 1000 ml/min. This gas flow is assumed to be laminar. The Reynolds number, given by $Re = \rho_{gas} v_{gas} \Delta / \mu_{gas}$ can be calculated here, with ρ_{gas} the gas density, v_{gas} the average gas velocity, μ_{gas} the gas dynamic viscosity and Δ a characteristic length. The average gas velocity is, for instance, for a gas flow of 1000 ml/min and the present geometric setup equal to about $v_{gas} = 0.11$ m/s. Taking the characteristic length the gas channel height ($\Delta = 3$ mm) and using the values from Table 1, we can estimate the Reynolds number for a gas flow of 1000 ml/min to be about 21. Even if we would take the characteristic length to be the gas channel length ($\Delta = 50$ mm), the Reynolds number would be about 356. Therefore, we can safely assume that the gas flow is laminar. The ambient (denoted by the subscript 'amb') conditions are at a temperature, T_{amb}, of 293.15 K and a pressure, p_{amb} of 1 atm. Surface deformation can be neglected if the capillary number is small ($Ca \ll 1$) and if the Galileo number is large ($Ga \gg 1$) "Colinet et al. (2001)". The first condition, irrespective of the second one (albeit the latter can also help if satisfied), ensures that the surface deformation is negligible for the finite wavenumber modes, whereas the second one guarantees the absence of low-wavenumber surface deformation modes of instability. The non-linear competition between these surface modes and the finite wave-length instability has already been studied in the literature "VanHook et al. (1995)". This discussion has also been lead in more details in "Machrafi et al. (2010)". Let us define the capillary and Galileo numbers in the liquid as $Ca = \mu_l \kappa_l / \gamma d_l$ and $Ga = g d_l^3 \rho_l / \mu_l \kappa_l$, with μ the dynamic viscosity, κ the thermal diffusivity, γ the surface tension, d_l the liquid thickness, g the gravity acceleration constant, ρ the density and the subscript "l" the designation that it concerns the liquid phase. It is then easy to show (using the data of Table 1) that for the thicknesses, considered in this work, both the conditions are satisfied. Hence, we can state that surface deformation can be neglected in this work.

The incompressible liquid and the gas phases are both described by the typical momentum (including buoyancy forces, i.e. Rayleigh effect), energy and species (only for the gas phase) balances. The Boussinesq approximation "Colinet et al. (2001)" will be adopted for both phases of the system, implying that the material properties of the fluids are treated as constant except for the density in the buoyancy terms, whose dependence on the temperature and mass fraction is taken in the following linearized form:

$$\rho_l \equiv \rho_l \{1 - \alpha_l (T_l - T_{l,0})\}, \tag{1}$$
$$\rho_g \equiv \rho_g \{1 - \alpha_g (T_g - T_{g,0}) - \varepsilon_g (\chi_g - \chi_{g,0})\}, \tag{2}$$

whereas the corresponding dependence on pressure is presumed to be negligible for the pressure range involved in the problem. Here, ρ is the density, T is the temperature, χ_g is the molar fraction of HFE-7100 in the gas, α and ε are the thermal and the solutal expansion coefficients. The subscripts *"l"* and *"g"* relate to the liquid and gas phases, respectively. The subscript *"0"* refers to a certain reference state (here taken to be the initial state). Clearly, the validity of different hypotheses underlying the Boussinesq approximation is limited to situations for which the temperature and mass fraction in the system remain close enough to the reference values introduced in (1) and (2). The following balance equations are used:

$$\nabla \cdot \vec{v}_l = 0 , \tag{3}$$

$$\rho_l \frac{\partial \vec{v}_l}{\partial t} = -\rho_l(\vec{v}_l \cdot \vec{\nabla})\vec{v}_l - \vec{\nabla}p_l + \mu_l\nabla^2\vec{v}_l + \rho_l\left(1 - \alpha_l(T_l - T_{l,0})\right)\vec{g} , \tag{4}$$

$$\frac{\partial T_l}{\partial t} = -(\vec{v}_l \cdot \vec{\nabla})T_l + \kappa_l\nabla^2T_l , \tag{5}$$

$$\nabla \cdot \vec{v}_g = 0 , \tag{6}$$

$$\rho_g \frac{\partial \vec{v}_g}{\partial t} = -\rho_g(\vec{v}_g \cdot \vec{\nabla})\vec{v}_g - \vec{\nabla}p_g + \mu_g\nabla^2\vec{v}_g + \rho_g\left(1 - \alpha_g(T_g - T_{g,0}) - \varepsilon_g(\chi_g - \chi_{g,0})\right)\vec{g} , \tag{7}$$

$$\frac{\partial T_g}{\partial t} = -(\vec{v}_g \cdot \vec{\nabla})T_g + \kappa_g\nabla^2T_g , \tag{8}$$

$$\frac{\partial \chi_g}{\partial t} = -(\vec{v}_g \cdot \vec{\nabla})\chi_g + D_g\nabla^2\chi_g , \tag{9}$$

where $\vec{v}$ and p are the (barycentric) velocity and pressure fields, respectively. Furthermore, D_g is the gas diffusion coefficient. Note that the thermal diffusivity κ is also defined by $\kappa = \lambda\,\rho^{-1}c_p^{-1}$, with λ and c_p being the thermal conductivity and heat capacity, respectively. For the liquid and gas phase respectively, (3) and (6) are the continuity equations for incompressible fluids, (4) and (7) are the momentum equations, (5) and (8) express the energy conservation, whereas (9) stands for the molar species balance equation of the vapor in the gas phase. In the gas phase, the Soret effect is neglected assuming small vapor concentration, in which limit this effect tends to disappear (and the same goes for the Dufour effect). It is also interesting to recall the following detailed expressions of the heat fluxes in the liquid and in the gas, as well as the molar flux in the gas, compatible with (5), (8) and (9):

$$\vec{q}_l = -\lambda_l\nabla T_l, \tag{10}$$

$$\vec{q}_g = -\lambda_g\,\nabla T_g, \tag{11}$$

$$\vec{J}_g = -\rho_g D_g\nabla\chi_g. \tag{12}$$

We continue with the boundary conditions. The walls confining the liquid are kept at the ambient temperature. The same goes for the bottom and top of the system. The gas flow enters the system at the ambient pressure and temperature. At the liquid-gas interface, we assume temperature continuity, velocity continuity (accounting for drag forces): $T_l = T_g$, $u_l = u_g$ and $v_l = v_g$, respectively. The Marangoni effect is accounted for via a tangential stress balance that takes account of the surface tension dependency on the temperature:

$$-\mu_g\left(\frac{\partial w_g}{\partial x} + \frac{\partial u_g}{\partial z}\right) + \mu_l\left(\frac{\partial w_l}{\partial x} + \frac{\partial u_l}{\partial z}\right) + \left(-\frac{\partial \gamma}{\partial T}\right)\frac{\partial T_l}{\partial x} = 0, \tag{13}$$

$$-\mu_g\left(\frac{\partial w_g}{\partial y} + \frac{\partial v_g}{\partial z}\right) + \mu_l\left(\frac{\partial w_l}{\partial y} + \frac{\partial v_l}{\partial z}\right) + \left(-\frac{\partial \gamma}{\partial T}\right)\frac{\partial T_l}{\partial y} = 0, \tag{14}$$

In (13) and (14), u, v and w are the components of the velocity vector in the coordinate directions x, y and z, respectively. The symbol γ stands for the surface tension.

The molar evaporation rate, J/M (with J the evaporation rate in kg/m^{2}s and M the molar mass), is given as the sum of a convective part, $J\chi_g/M$ and a diffusive part, $-n_g D_g \frac{\partial \chi_g}{\partial z}$ (with the n_g the molar density of the vapor in the gas phase). From this, one can deduce the following expression for the evaporation rate

$$J = -\frac{n_g D_g M}{1-\chi_g} \frac{\partial \chi_g}{\partial z}.$$ (15)

The evaporation process is described by assuming a local thermodynamic equilibrium, where the vapor concentration at the liquid-gas interface, $\chi_{g\Sigma}$, is given in terms of the saturation pressure p_{sat}, the latter being temperature-dependent via the Clausius-Clapeyron relation for ideal gases. One thus has

$$\chi_{g\Sigma} = \frac{p_{sat}(T_\Sigma)}{p_{amb}} = \frac{p_{sat}(T_{amb})}{p_{amb}} e^{\left(-\frac{LM}{R}\left(\frac{1}{T_\Sigma}-\frac{1}{T_{amb}}\right)\right)},$$ (16)

with L the latent heat of evaporation, R the universal gas constant and the subscript 'Σ' indicating that it concerns the liquid-gas interface. The relation between the temperature and the evaporation rate is given by the energy balance at the liquid-gas interface,

$$-\lambda_l \frac{\partial T_l}{\partial z} + \lambda_g \frac{\partial T_g}{\partial z} = JL.$$ (17)

Eq. (16) explains how the vapor molar fraction at the interface is related to the temperature at the interface. Together with Eq. (15), we can relate the molar fraction of the vapor with the temperature at the interface. This is, however, not sufficient to explain the cooling effect, since at this moment the interface temperature (T_Σ) is still unknown (together with $\chi_{g\Sigma}$, and J). Via Eq. (17), we can obtain mathematical closure and relate finally the vapor molar fraction to the temperature gradient in the liquid. We end up with the solution of $\chi_{g\Sigma}$, T_Σ and J (knowing the values of the molar fraction and temperature at the top and bottom boundaries, respectively) by solving simultaneously for Eqs. (15) through (17), finding thereby the relation between the mass flux and the cooling at the interface.

The system will be initially at rest ($\vec{v}_l = \vec{v}_g = 0$), with a uniform temperature equal to that of the ambient conditions ($T_l = T_g = T_{amb}$). The gas in the gas channel is initially without vapor ($\chi_g = 0$). The initial conditions merit a discussion, since they can influence the behavior of the heat flux. The heat flux is influenced mainly due to the vapor content in the gas channel. A higher vapor content means a lower concentration gradient at the liquid-gas interface and a lower evaporation flux, hence a lower heat flux. Other ways to influence the heat flux is to change the ambient temperature or pressure. The heat flux depends also on the flow parameters. Indeed, a higher flow rate will increase the evaporation flux and therefore also the heat flux. However, it is not the purpose of this paper to perform a parametric study of the influence of the initial conditions and are subject to future study.

The model presented in this section is applied using a specific case of a HFE-7100 liquid evaporating into a nitrogen gas flow. The physical properties of the fluids used in the simulations (both for the typical bulk equations and the boundary conditions) are given in Table 1.

Table 1 Physical properties of the HFE-7100/nitrogen system "Machrafi et al. (2013b)".[a]

Symbol	Physical property	Value in the liquid phase	Value in the gas phase
ρ [kg/m^3]	Density	$1.482*10^3$	1.145
c_p [J/kgK]	Heat capacity	$1.183*10^3$	$1.039*10^3$
λ [W/Km]	Thermal conductivity	$6.9*10^{-2}$	$2.59*10^{-2}$
μ [Pas]	Dynamic viscosity	$5.8*10^{-4}$	$1.77*10^{-5}$

D_g [m²/s]	Diffusion coefficient in the gas	6.98×10^{-6}
γ_T [N/Km]	T-derivative of surface tension	-1.14×10^{-4}
p_{sat} [bar]	Saturation pressure	2.69×10^{-1}
L [J/kg]	Latent heat of evaporation	1.116×10^{5}
κ_l [m²/s]	Thermal diffusivity	3.94×10^{-8}
γ [N/m]	Surface tension	13.6×10^{-3}
g [m/s²]	Gravity acceleration	9.81
α_l [1/K]	Thermal expansion coefficient	1.8×10^{-3}

[a]The subscript "l" stands for "in the liquid"

2.2 On the numerical part

In this subsection, we will give more insight into the numerical part used in this work. ComSol uses the finite element method (FEM). This method is based on discretizing the calculation domain into several elements. Subdividing the domain of interest into finite elements allows denoting a generic element where the dependent variables are approximated at nodal points through interpolation functions. Connecting these elements to one another creates a mesh. In this work, we connected the elements in such a way that we have tetrahedral meshes, which appears to give the most stable configuration for fluid flow. The meshing at the liquid-gas interface is the densest one, where the most complicated fluid physics occurs. The mesh density at the interface itself is 6 elements per mm for the 2D case and 32 elements per mm² for the 3D case. Depending on whether we deal with the 2D or 3D case, the equations multiplied by the interpolation function (in our case, we opted for quadratic ones) are integrated over a surface part of the mesh or a volume part of the mesh, respectively. After some manipulations, including the use of integration by parts and Green's theorem for the higher order derivatives, we obtain element matrix equations for each element. The same is done for the boundary conditions. The solutions are then found by solving for the matrices (by LU factorization). More information about these procedures can be found in, for instance, "Li et al. (1999)".

The solver is a fully coupled solver that solves the governing equations simultaneously as a set, or vector, of equations. A variable time stepping is used, depending on the convergence of the iterations at each time step. A relative convergence criterion of 10^{-4} is maintained. The optimization of the mesh has been done by using simple Poiseuille flow. It appeared from earlier work of one of the authors "Iorio (2006)" that for this simple Poiseuille flow, the mesh is optimized with 40000 meshing points (comparing the theoretically calculated average velocity of Poiseuille flow in the cimex configuration to the simulated one, accepting a relative difference of less than 10^{-4}). In the present work, we deal with 150126 meshing points or elements for the 2D model and with 185247 elements for the 3D model. Therefore, we consider our mesh to be optimized. Also, we study the convergence and validation of the numerical simulations. We have calculated the average evaporation flux (kg/m²s) at $t = 10$s as a function of the number of elements at the liquid-gas interface. It appears that the average evaporation flux was within a relative difference of 10^{-4} between 57878 and 150126 elements. We still opted for 150126 elements, since this gave more precise pattern visualization, respecting a reasonable computing time (< 4 days), using an AMD Opteron Processor with 128 GB memory.

3. Fluid flow into the bulk liquid

In this section, we comment on 2D simulations that have been performed, where we investigate qualitatively the fluid flow into the bulk liquid for a gas flow rate of 100 ml/min. We also study the effect of the liquid thickness on the fluid flow, varying it from 2 to 8 mm. The results are presented in Figs. 2 to 4 as temperature grayscale-surface-plots, where the added solid lines represent qualitatively flow patterns (the absolute values of the temperature and the streamlines are here not of importance).

Fig. 2 shows for the three liquid thicknesses considered in this work the results at t = 0.1s. We can see that the streamlines are quasi-horizontal (with the exception of some starting instability rolls), which indicates the flow of the liquid due to the shear effect of the gas flow. At this instant, the maximum horizontal velocity at the liquid-gas interface is only about $8.3*10^{-6}$ m/s. This is negligible in comparison with the average gas velocity of 0.011 m/s. Moreover, the gas viscosity is much lower than the liquid one. Furthermore, on the left of the liquid-gas opening, there is a cover, along which we have in the gas channel a Hagen-Poiseuille flow, so that the velocity (no slip at the wall) is zero at the cover. In consideration of these observations, we can state that the drag force in the present setup is of negligible importance even at gas flows of 1000 ml/min. As time proceeds, we can see in Figs. 3 and 4 that these quasi-horizontal streamlines are no longer visible. This is because the density of the streamlines has been reduced so that they would be clearly distinguishable. The streamlines due to the shear effect of the gas flow, being of much less density, are therefore not displayed by the postprocessor of the program in the cases of Figs. 3 and 4. Moreover, Fig. 5 presents at t=10s the horizontal (in gas-flow direction) velocities in the gas, 0.05 mm above the interface, in the liquid, 0.05 mm under the interface, and at the interface itself as a function of the x-coordinate of the interface opening (an x-coordinate of 0 mm stands for the left border of the opening and an x-coordinate of 10.6 mm stands for the right border of the opening). Fig. 5 shows us that at the left border of the opening (and 0.05 mm above it) the velocity in the gas has a velocity of about 0.025 m/s (note the average velocity in the gas channel of about 0.11 m/s) and at the right border less than 0.01 m/s. Indeed, in between the borders, the velocity in the gas becomes larger than its entering velocity and becomes even negative. Furthermore, if the gas flow was to influence the liquid flow by shear, the gas velocity would, not increase and certainly not become negative. This implies that it is the gas that is influenced by the liquid flow (which shows both positive and negative velocities) and not the contrary. From the results in Fig. 3, we can observe that time t = 1s, for the 3 liquid thicknesses considered, first several small rolls are formed near the surface, caused by the surface-tension. Fig. 4 shows the corresponding results at time t = 10s. As time proceeds, the rolls grow towards the bottom of the liquid layer. The rolls also grow in horizontal direction merging with each other until a stable configuration is obtained. For a higher liquid layer thickness, the merging occurs earlier and less rolls are left at t = 10s. Note here, that we have noticed that this merging occurs at about 4-5s and that thereafter the structure of the rolls does not change. We, therefore, do not expect a significant change of the structure of the rolls beyond 10s. Furthermore, the temperature gradients decrease as the liquid thickness increases, which is caused by the larger liquid thickness for the same temperature difference across the liquid layer. Moreover, the rolls extend more horizontally under the cover towards the side walls as the liquid layer thickness increases. For smaller liquid layer thicknesses, the rolls reach the bottom where a constant temperature of 298.15 K is maintained. Therefore the rolls stay concentrated close to the interface. As the liquid layer thickness increases, the rolls have more time to increase in size towards the side walls before they reach the bottom of the liquid layer. It appears also from Figs. 3 and 4 that the rolls expand further to the left than to the right side of the setup. We have established that the drag force is of little influence on the cells, with respect to the Marangoni flow. Now, the gas coming from the left does not contain any vapor. Due to evaporation, the right border will have a certain amount of vapor above it. Therefore, a larger concentration gradient exists at the left border of the liquid-gas interface. Therefore, the mass flux will there be higher as well (see also Eq. (15)). This causes higher temperature gradients at the left border (see also Eq. (17)), which increases the Marangoni convection. Therefore, the cells are bigger at the left side. Note that Fig. 2 already shows that small rolls are formed at the left side and not at the right side of the liquid-gas interface.
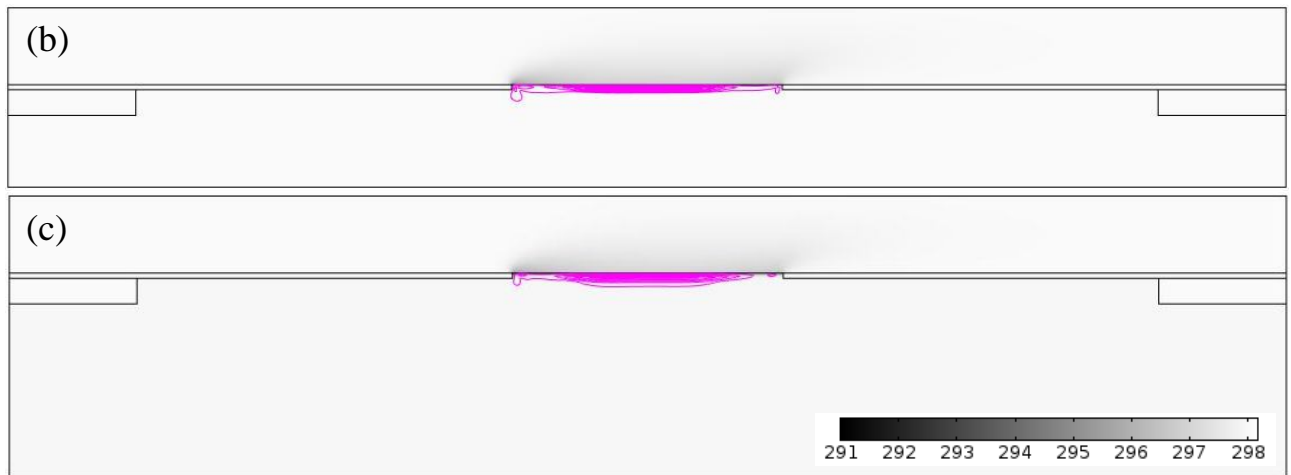

(a)

Fig. 2 Temperatures in gray-scale (legend given in K) and streamlines for t = 0.1s. Liquid thicknesses of (a) 2 mm, (b) 4 mm and (c) 8 mm with a gas flow of 100 ml/min.
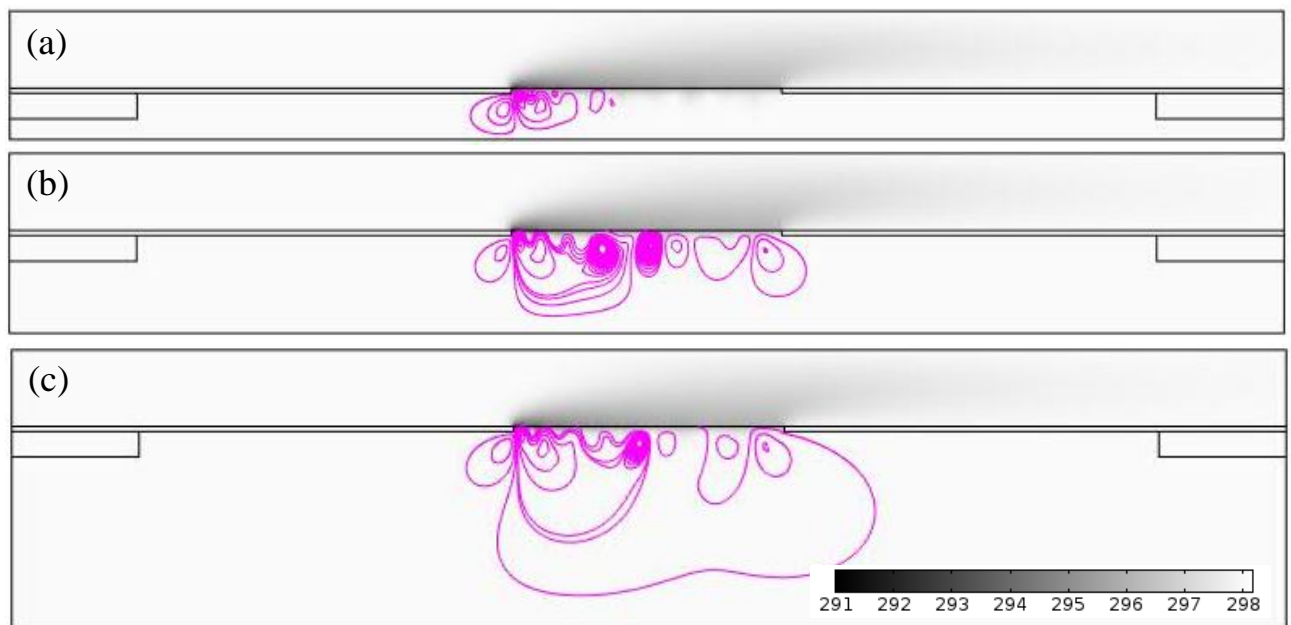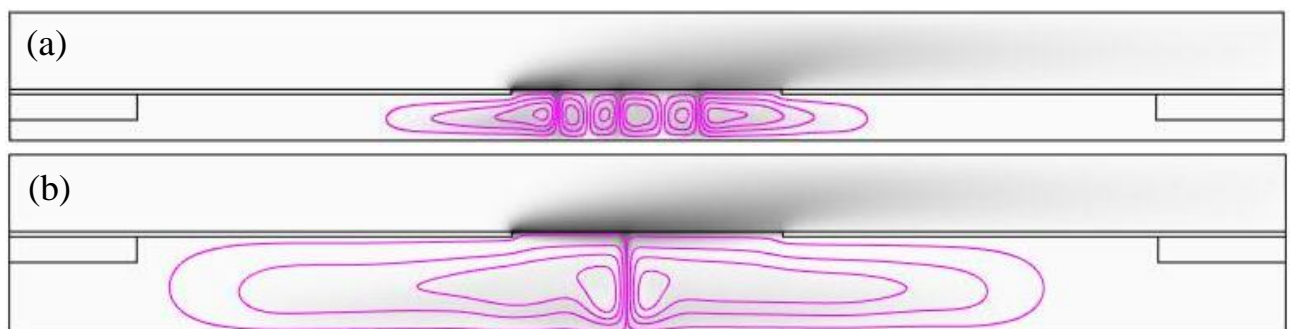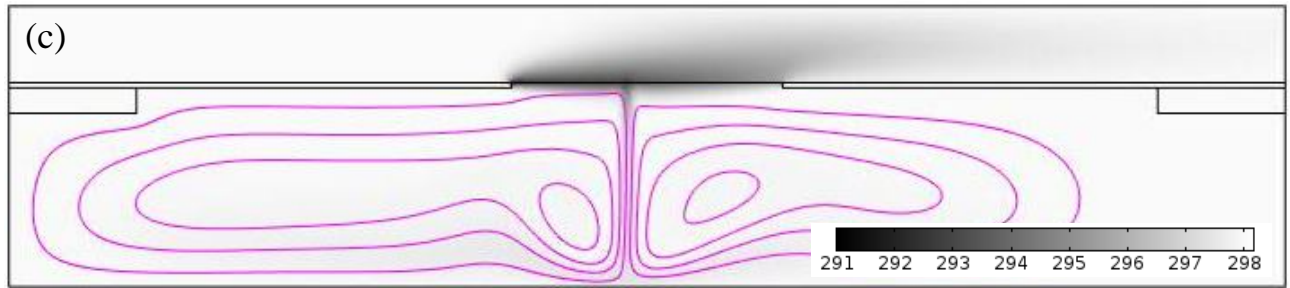

Fig. 3 Temperatures in gray-scale (legend given in K) and streamlines for t = 1s. Liquid thicknesses of (a) 2 mm, (b) 4 mm and (c) 8 mm with a gas flow of 100 ml/min.

Fig. 4 Temperatures in gray-scale (legend given in K) and streamlines for t = 10s. Liquid thicknesses of (a) 2 mm, (b) 4 mm and (c) 8 mm with a gas flow of 100 ml/min.
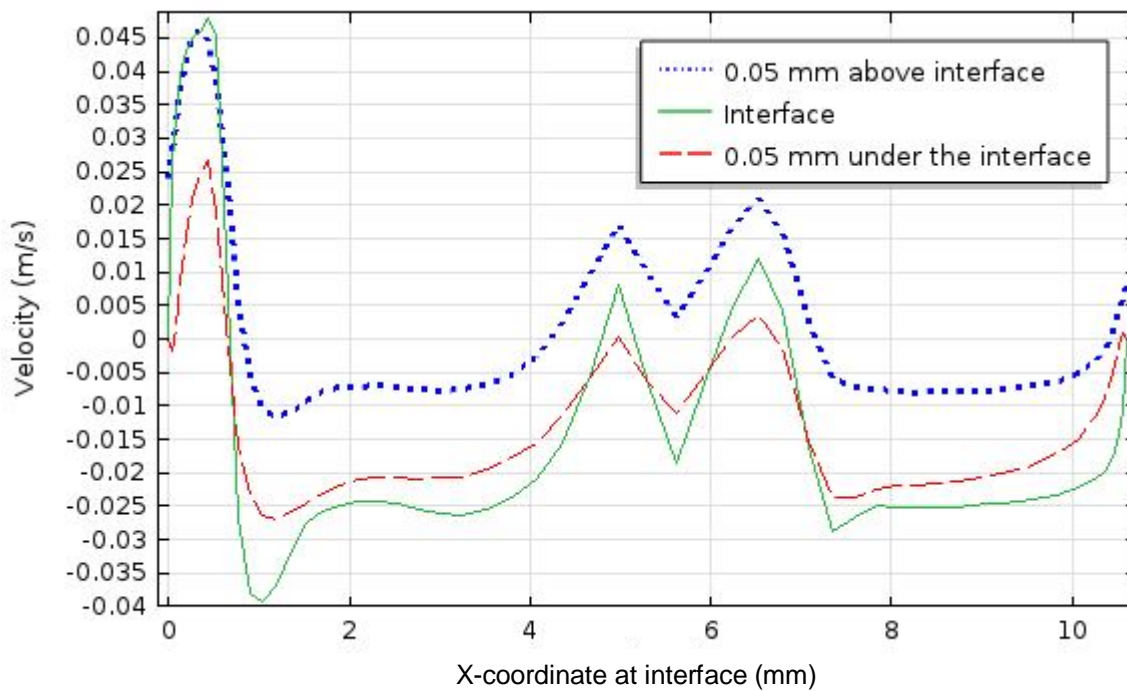

Fig. 5 Velocity of fluid flow in the gas (0.05 mm above the interface), at the level of the interface and in the liquid (0.05 mm under the interface) with a liquid thickness of 2 mm and a gas flow of 1000 ml/min at t=10s.

4. Pattern formation and heat flux at the liquid-gas interface

In this section, we discuss 3D simulations that have been performed for a gas flow of 1000 ml/min. We are interested in the patterns on the upper surface as function of time, and their relations with the heat flux through the liquid-gas interface. The images shown in Fig. 5 are top views of the liquid-gas and the shaded plots represent the calculated temperature field.
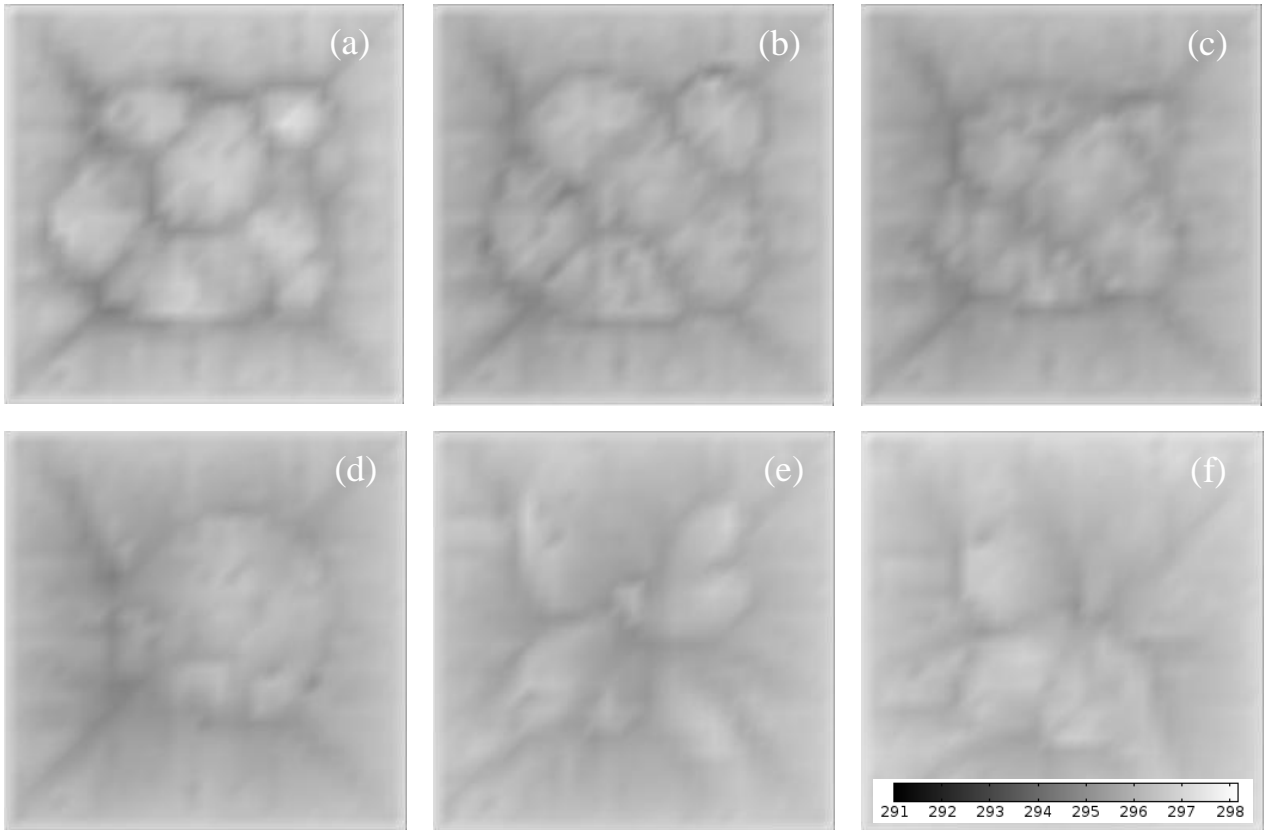
Fig. 6 Temperatures (legend given in K) with a gas flow of 1000 ml/min and a liquid thickness of 2 mm at (a) t = 0.2 s, (b) t = 0.4 s, (c) t = 0.6 s, (d) t = 1 s, (e) t = 3 s and (f) t = 10 s.

We can see that in the beginning (Fig. 6(a)-(c)) the cells have certain distinguishable forms that are of quasi-circular form being spatially quasi-symmetric. As time proceeds, the cells become asymmetric and the cell sizes differ a lot more from one to another. It is now interesting to trace the heat flux versus the time in Fig. 6 and compare it qualitatively to the images in Fig. 4.
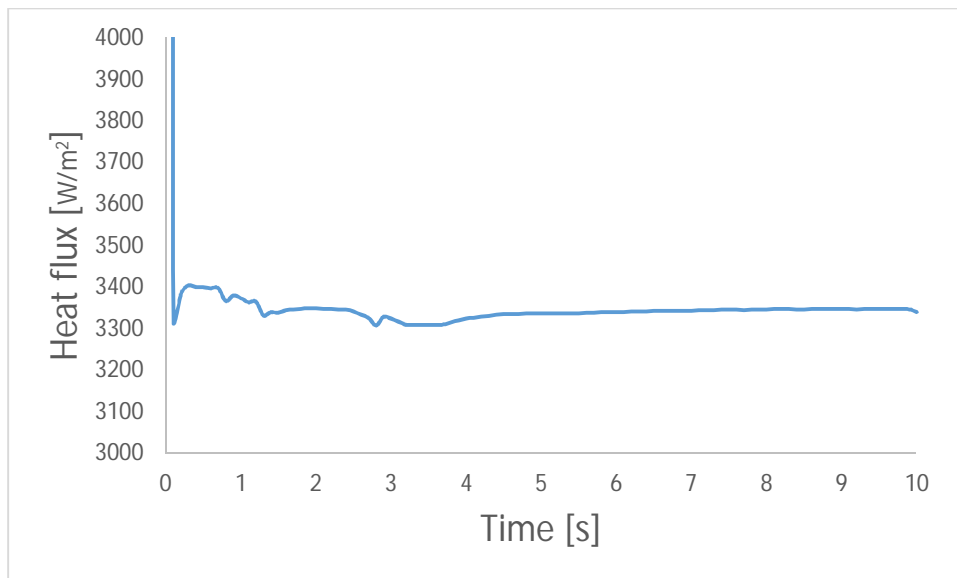

Fig. 7 Heat flux versus the time with a gas flow of 1000 ml/min and a liquid thickness of 2 mm.

First of all, we can see that the heat flux is rather high at the beginning, followed by a pronounced minimum. This can be explained by the singularity that occurs at the beginning. In fact, the simulation starts with a zero concentration in the bulk of the gas phase, but the concentration along the liquid-gas interface is not zero due to the assumption of a local thermodynamic equilibrium (see Eq. (16)),

which imposes a non-zero concentration related to the saturation pressure of HFE-7100 vapor. Therefore, the evaporation rate (15) is quite high in the very beginning of the calculations, but we will mainly concentrate on the behavior of the system after this short period. Note that a detailed discussion about the singularity just described can be found in "Machrafi et al. (2013a)", albeit for a binary mixture. It is also interesting to mention that in a real physical experiment, such as the one performed by "Lyulin and Kabov (2014)", other effects are important for the initial conditions. We can think of the filling of the liquid container and the starting of the evaporation loop. Incorporating these effects here would result into an unacceptable computing time in consideration of the information that would be gained from the simulation. Therefore, a full comparison with the experiment is not of interest here.

As time proceeds, we can see that indeed small fluctuations are visible corresponding to the formation of the patterns (in Fig. 6 (a), (b) and (c)), which are of symmetric shape with comparable sizes. These fluctuations attenuate as time proceeds and after the formation of non-symmetric cells with distinct shapes and sizes (in Fig. 6 (e) and (f)). All in all, we can say, however, that even if these fluctuations are visible, the heat flux follows a quasi-monotonic behavior towards a constant value. This seems to suggest that at short scales there is a relation to be found between patterns and heat flux, but that eventually the overall heat flux is of importance, which does not depend on the type of patterns. Our results are compared to an experiment in "Lyulin and Kabov (2014)", where they performed a study using a complete loop with evaporator and heat exchanger. We only focus here on the evaporator. Note, therefore, that it is not our purpose to make a full comparison with their experimental study, but rather give an example of a good comparison to show the reliability of our model. The results in "Lyulin and Kabov (2014)" are presented as evaporation fluxes versus the liquid thickness for several average gas velocities. A gas flow of 1000 ml/min corresponds here to an average gas velocity of 0.11 m/s. With this gas velocity, we can extract from "Lyulin and Kabov (2014)" (taking into account the cooling at the liquid-gas interface), an experimental evaporation flux of ~0.031 ± 0.003. Multiplying this by the latent heat of evaporation gives us an approximate experimental heat flux of ~3460 ± 330 W/m², which agrees well with our simulation, presented in Fig. 7.

5. Conclusions

In this work, we studied the fluid flow into a bulk HFE-7100 liquid evaporating into a nitrogen gas flow by means of two and three-dimensional numerical simulations. We observed also the behavior of patterns at the liquid-gas interface and its relation with the heat flux by means of three-dimensional numerical simulations.

The nitrogen gas flow in the physical system, based on an experimental setup, is either 100 or 1000 ml/min. The liquid thickness can be varied between 2 and 8 mm. The two-dimensional results show that first several small rolls are formed near the surface, caused most probably by the surface-tension effect. The rolls grow towards the bottom of the liquid layer. As time proceeds, buoyancy becomes more important. However, we cannot say for sure whether the growth of the rolls towards the bottom of the liquid layer is due to the buoyancy or the surface tension effect. In "Colinet et al. (2001)" a dynamic Bond number, Bo_d, is defined standing for the ratio of buoyancy and surface tension effects. This dynamic Bond number is proportional to the square of a certain characteristic length, δ_l. In other words, $Bo_d \sim \delta_l^2$. Since, we cope with a transient process, it is convenient to choose this characteristic length to be the thickness of a diffusive thermal boundary layer. Due to the gas flow, we have said that the evaporation rate is not the same at the left and right borders of the liquid-gas interface. Therefore, the thermal boundary layer will not be the same across the width of the liquid-gas interface. Nonetheless, we can say that δ_l will have the order of magnitude of $\sqrt{\kappa_l t}$. Now, we can make a qualitative remark about the analysis buoyancy versus surface tension. This analysis shows that for small times the thermal boundary layer will be small, hence a small dynamic Bond number, the instability generating the rolls being mainly caused by the surface tension effect (also referred to as

the Marangoni effect). As time proceeds, the thermal boundary layer will grow and the dynamic Bond number as well. We can then say that instability will be mainly due to buoyancy effects (also referred to as the Rayleigh effect). In order to find a quantitative criterion, a simulation experiment should be performed, where we neglect on one side the buoyancy effect and evaluate the fluid flow (for which some criteria can be used, such as interface velocity or evaporation rate) over time, and neglect on the other side the surface tension effect and evaluate again the fluid flow. Subsequently, this should be compared to the fluid flow over time, taking in to account both the buoyancy and surface tension effects. This is, however, beyond the scope of this work and is subject to future work.

The three-dimensional results show that at first, the developing patterns influence the heat flux. It has been shown that in the very beginning of the evaporation process ($t < 2$s), slight oscillations take place in the heat flux. However, very soon ($t > 4$s), the heat flux reaches a quasi-monotonic behavior that does not depend greatly on the different patterns, being associated to a transition from symmetrically shaped patterns to patterns with shape asymmetry.

Acknowledgments

References

Bénard, H., (1901) Les tourbillons cellulaires dans une nappe liquide transportant de la chaleur en régime permanent, *Ann. Chem. Phys.*, 23, pp. 62-144.

Bestehorn, M., Merkt, D., (2006) Regular Surface Patterns on Rayleigh-Taylor Unstable Evaporating Films Heated from Below, *Phys. Rev. Lett.*, 97, 127802.

Bestehorn, M., (2007) Convection in thick and in thin fluid layers with a free surface – The influence of evaporation, *Eur. Phys. J.S.T.*, 146, pp. 391-405.

Bodenschatz, E., Pesch, W., Ahlers, G., (2000) Recent developments in Rayleigh–Bénard convection, *Annu. Rev. Fluid Mech.*, 32, 709-778.

Colinet, P., Legros, J.C., Velarde, M.G., (2001) *Non Linear Dynamics of Surface Tension Driven Instabilities*, Berlin: Wiley-VCH Verlag.

Drazin, P., Reid, W.H., (1981) *Hydrodynamic Stability,* Cambridge: Cambridge University Press.

Goncharova, O.N., Hennenberg, M., Rezanova, E.V., Kabov, O.A., (2013) Modeling of the Convective Fluid Flows with Evaporation in the Two-Layer Systems, *Interfac. Phenom. Heat Transf.*, 1, pp. 317–338.

Iorio, C.S., (2006) *Experimental and numerical study of the coupling between evaporation and thermocapillarity*, PhD thesis, pp. 80-82.

Iorio, C.S., Goncharova, O., Kabov, O., (2011) Heat and mass transfer control by evaporative thermal pattering of thin liquid layers, *Comput. Therm. Sc.*, 3, pp. 333-342.

Li, Y.S., Liu, S.-X., Yu, Y.-X., Lai, G.-Z., (1999) Numerical modeling of Boussinesq equations by finite element method, *Coastal Eng.,* 37, pp. 97–122

Lyulin, Y., Kabov, O., (2014) Evaporative convection in a horizontal liquid layer under shear–stress gas flow, *Intern. J. Heat Mass Transf.*, 70, 599-609.

Machrafi, H., Rednikov, A., Colinet, P., Dauby, P.C., (2010) Bénard instabilities in a binary-liquid layer evaporating into an inert gas, *J. Coll. Interface*, 349, pp. 331-353.

Machrafi, H., Rednikov, A., Colinet, P., Dauby, P.C., (2013a) Time-dependent Marangoni-Bénard instability of an evaporating binary-liquid layer including gas transients, *Phys. Fluids*, 25, 084106.

Machrafi, H., Sadoun, N., Rednikov, A., Dehaeck, S., Dauby, P.C., Colinet, P., (2013b) Evaporation Rates and Bénard-Marangoni Supercriticality Levels for Liquid Layers Under an Inert Gas Flow, *Micrograv. Sc. Tech.*, 25, pp. 251-265.

Pearson, J.R.A., (1958) On convection cells induced by surface tension, *J. Fluid Mech.*, 4, pp. 489-500.

VanHook, S.A., Schatz, M.F., McCormick, W.D., Swift, J.B., Swinney, H.L., (1995) Long-wavelength instability in surface-tension-driven Bénard convection, *Phys. Rev. Lett.*, 75, pp. 4397.